2024 IEEE/RSJ International Conference on Intelligent Robots and Systems (IROS)
October 14-18, 2024. Abu Dhabi, UAE

Biodegradable Gliding Paper Flyers Fabricated Through Inkjet Printing

Luca Girardi[1,2]*, Rui Wu[1,2], Yuki Fukatsu[3], Hiroki Shigemune[3] and Stefano Mintchev[1,2]

***Abstract*— Seed-inspired minimalist microflyers are showing potential as dispersal platforms for sensor networks and seeds. Their function relies on the sheer number of low-cost flyers, inevitably raising concerns about the post-operation environmental impact. We propose a biodegradable paper glider platform fabricated through origami inkjet printing. This method can fold origami along printing patterns on different paper varieties. We created a printing pattern that allows 2D paper sheets to self-fold into a 3D flying wing glider with designable wing geometry and center of gravity (CG). The design allows stable and repeatable gliding behavior, proven in our gliding tests. It successfully achieves the dispersal of multiple gliders from a hovering drone, covering an average horizontal distance larger than the release height. We also tested the biodegradation of different paper types compatible with the printing method, showing near-complete degradation after 15 weeks in moist soil. Our study presents a novel, potentially scalable approach for fabricating environmentally friendly microflyers, offering new avenues for remote environmental sensing and automated forest restoration programs.**

I. Introduction

Nature adopts passive flight for seed dispersal, which employs wings or bristles to generate aerodynamic forces that prolong descent time, and utilises wind to maximize dispersal distance [1], [2]. This has inspired the design of minimalist microflyers that achieve long-distance coverage at a low cost for applications such as the deployment of sensor networks for monitoring pollutants and environmental parameters [3], [4], and artificial seed dispersal [5]. A large variety of designs have been proposed for such seed-inspired microflyers. These include dandelion-like parachute flyers with drag-generating surfaces [3], [6], auto-rotating flyers inspired by maple seeds that generate lift by auto-rotating during descent [7], [8], [9], [10], and others harnessing a gliding flight that resembles that of the Javan cucumber seed (*Alsomitra macrocarpa*) [11].

These microflyers are often not retrievable after deployment due to their widespread dispersal, underscoring the importance of minimizing non-degradable waste after the end of their use. This concern has promoted the interest toward biodegradable structures and electronics, aiming to make the system environmentally friendly [4], [12], [13]. Wiesemüller et al. have reported a biodegradable glider fabricated from potato starch wafer paper through wet molding, which has a wing inspired by Javan cucumber seed, and measures rainwater acidity using a Litmus patch [11]. Yoon et al. have developed a biodegradable auto-rotating flyer with a main body made from lactide-co-glycolide film, and cellulose-based chemical indicators to measure pH, UV radiation, and heavy metal concentrations [14]. Cikalleshi et al. have developed an auto-rotating flyer 3D printed from biodegradable polylactic acid polymer, which closely mimics the characteristics of a maple seed and monitors environmental temperature through thermometric fluorescence [15]. The key to realizing such microflyers lies in the biodegradability of the structural material and the shape-forming process to enable a potentially scalable and cost-effective fabrication of flyers with tailored aerodynamic properties.

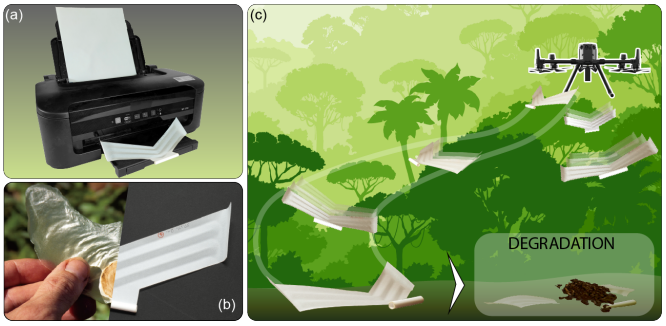

Fig. 1. Printable biodegradable flyers. (a) Novel fabrication method for self-folding biodegradable paper gliders through inkjet printing. (b) Comparison of the glider's geometry with that of a Javan cucumber seed; photograph adapted from [20]. (c) Schematics of the outdoor deployment life-cycle of the biodegradable paper gliders.

We propose a new method to fabricate biodegradable flying wings through print-induced paper folding via inkjet printing [16] (Fig. 1a). It utilizes the adsorption-induced swelling effect of water-based ink to induce permanent folding of the paper [17], [18], thereby introducing a 3D glider geometry with a desirable wing twist, CG, and enhanced rigidity, all crucial to the stable and reliable gliding flight. The method is compatible with a wide variety of papers, and thus can exploit the rich heritage of paper-like materials that are naturally biodegradable [19].

To demonstrate this fabrication method, we have designed a printing pattern to realize a flying wing with geometry inspired by the Javan cucumber seed (Fig. 1b), with wing twist and CG position adjusted through pattern parameters. The gliders are fabricated from biodegradable tracing paper, and tested to identify design parameters that achieve trimmed

This work was supported by the Swiss National Science Foundation through the Eccellenza Grant (grant number 186865), the ETH Zurich Research Grants (grant number ETH-15 20-2), and the JSPS KAKENHI Grant (grant number JP22K14226)

[1]Environmental Robotics Laboratory, Department of Environmental Systems Science, ETH Zurich, 8092 Zurich, Switzerland

[2]Swiss Federal Institute for Forest, Snow and Landscape Research (WSL), 8903 Birmensdorf, Switzerland

[3]Department of Electrical Engineering, Shibaura Institute of Technology, Tokyo 135-8548, Japan

*Corresponding author: girardil@ethz.ch

flight with prolonged duration. Six gliders are then deployed from a drone platform, demonstrating its potential as a cost-effective biodegradable flyer for widespread aerial dispersal (Fig. 1c). Soil-based biodegradability tests are also conducted to quantitatively validate the degradation of several types of papers compatible with the printing method.

II. Inkjet Printing for Self-Folding Flyers

The fabrication of the flying wing is based on inkjet printing-induced self-folding to produce the 3D geometrical features crucial for achieving aerodynamic, inertial, and flexural stability essential for stable flight. The geometry of the flyer is inspired by the Javan cucumber seed (see Fig. 1b), featuring an aspect ratio (AR) of 3.9, a 25° sweepback angle, and a 200 mm wingspan. The 2D base geometry is laser-cut from a sheet of the chosen variety of paper. The method employed for incorporating permanent self-folding patterns is analogous to the self-folding through inkjet printing introduced in [16] and schematized in Fig. 2a. Printing is done with an Epson WorkForce WF-2110W inkjet printer using modified cartridges loaded with self-folding ink as the one utilized in [18]. Fig. 2b illustrates the two-sided printing pattern utilized to impart the necessary 3D shape to the 2D base geometry of the flyer. To allow printing of the pattern on both sides, the cutout is fixed with 3M Scotch Crystal tape to an A4 printing paper substrate. The creases corresponding to the valley folds (blue regions in the figure) are printed first, releasing the cutout immediately after the end of the print to let the folding pattern develop unconstrained.

As described in [16], the development lasts ∼10 min, a sufficient time frame to allow printing the full pattern without altering the target folding pattern. After 10 min, the cutout is fixed to the substrate on the opposite side to print the mountain folds and the nose coil (red regions in the figure).

A. Aerodynamic Design Requirements

Among flying seeds, the Javan cucumber one shows exceptional gliding performance [21] owing to its wing-like shape, featuring a swept-back planform and upward-bent wing tips, and to the anteriorized CG position relative to its aerodynamic center (AC) [22]. To achieve a stable flight, a flying wing like the Javan Cucumber seed necessitates specific inertial, aerodynamic, and structural properties determined by the 3D geometry and mass distribution of the wing. A sweepback angle in the planform enhances directional and roll stability [23]. In flying wings, the CG needs to be anterior to the AC to initiate forward gliding, otherwise, the flyer will enter a swaying or tumbling motion typical of free-falling flat sheets of paper [24], [25], [26], [27] (see Fig. 2d). The wing's net lift acts on the AC, thereby generating a pitching-down moment because of the anteriorized position of the CG. For longitudinal stability, this moment needs to be counterbalanced by a nose-up aerodynamic pitching moment acting on the airfoil as the glide speed increases [23]. On a flying wing, this can be achieved by twisting the outermost wing sections downward (see Fig. 2c). Furthermore, the directional stability of flying wings can be improved by winglets [23]. Finally, due to lift forces, spanwise flexural rigidity is essential to avoid excessive and potentially destabilizing aeroelastic wing flex. The following sections

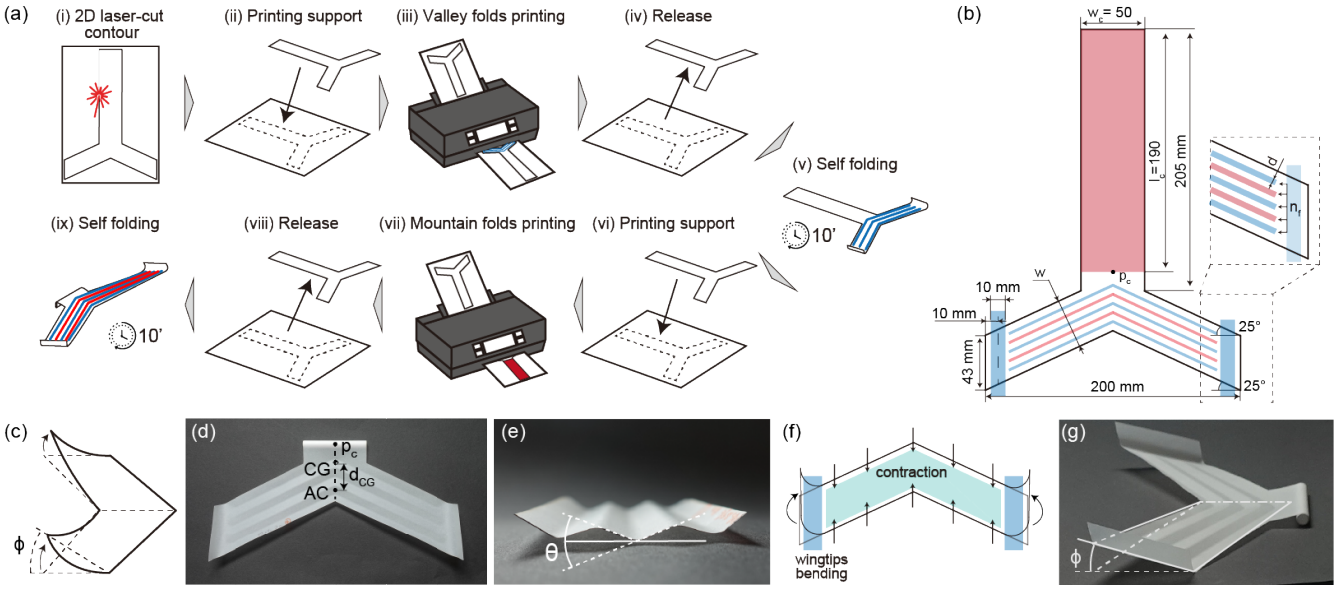

Fig. 2. Fabrication and design features of the self-folding glider. (a) Method for fabricating the self-folding paper gliders through inkjet printing. (b) Dimensions of the base 2D geometry of the glider (contour) and two-sided printing pattern for self-folding (colored regions). Valley folds are in blue and mountain folds are in red. (c) Illustration of the wing twist angle Φ. (d) Top view of a glider fabricated with 82 µm-thick tracing paper and d = 2 mm-wide printing lines with an indication of the CG, AC, and p_c positions and of the distance d_{CG}. (e) Effect of the 'zigzag' folding pattern on an unconstrained sectioned portion of the wing with an indication of the fold angle θ. (f) Illustration of the chordwise contraction effect of the zigzag folding pattern and the upward bending of the wingtips to induce the kinematic constraint. (g) Side view of the same glider as in (d) showing the formation of winglets and the arising wing twist Φ.

illustrate how all the design requirements described above are attained by the proposed paper glider design through a tailored selection of the 2D paper geometry and its self-folding printing pattern.

B. CG Positioning Through Self-Folding

As previously discussed, a strategy for designing the CG position relative to the AC is crucial for longitudinal stability. To address this, a rectangular strip has been integrated into the nose of the 2D flyer's cutout (see Fig. 2b). By uniformly printing over the foremost section of this strip, it naturally curls into a coil (visible in Fig. 2g). The mass of the coil, and consequently the CG position, can be finely tuned by adjusting the length of the strip (l_c). This provides a method to design the advancement of the CG relative to the AC, which has an impact on the longitudinal flight stability.

The longitudinal distance d_{CG} from CG to AC as a function of l_c, in millimeters, is calculated with Equation 1:

$$d_{CG}(l_c) = \frac{d_{CG,0} \cdot A_0 + d_c \cdot w_c l_c}{A_0 + w_c l_c} \simeq \frac{1203 + 50\, l_c}{185 + l_c}, \qquad (1)$$

where $d_{CG,0}$ = 6.5 mm is the CG-to-AC distance in a coil-less flyer of wing surface A_0 = 9 254 mm^2, d_c = 49.7 mm is the longitudinal distance from AC to the coil center, and w_c = 50 mm is the strip width (see Fig. 2d). Admissible values for l_c are in the range [0, 190] mm. In the results section, we show how trimming the length of the coil leads to the longest flight duration.

C. Wing Twisting Through Self-Folding

Twisting the wing to reduce the tip's angle of attack relative to the root generates a downforce on the wingtip region. On a swept-back wing, this downforce acts aft of the AC, thus generating the nose-up pitching moment essential for longitudinal stability as previously discussed. The twist angle Φ is defined as the angle between the root and tip chord, as indicated in Fig. 2c,g. This geometric feature is achieved through a folding pattern consisting of alternating mountain and valley folds parallel to the wing edges, along with two chordwise valley folds at the wingtips. As illustrated in Fig. 2c, the alternating pattern is obtained by printing lines of adjustable width d, while the chordwise folds are obtained with a 10 mm-wide printing line. These upward-bending folds additionally form vertical fins at the wingtips that act as winglets and contribute to the glider's directional stability (see Fig. 2f-g).

The alternating folds induce a 'zigzag' folding pattern in the main body of the flying wing, resulting in chordwise contraction as shown in Fig. 2e-f. The wing twist is introduced by constraining the chordwise shrinkage with the two chordwise winglet creases (Fig. 2f-g). As the zigzag pattern naturally tends toward its shrunk minimum internal energy state, this constraint increases the elastic potential energy stored in the flyer's structure. The flyer exhibits three stable states at this heightened energy state, all with twisted wings. Among these, only one stable state features a symmetrical twist on both wings, as visible in Fig. 2d,g. The remaining states are not considered as they exhibit an anti-symmetric wing twist, which would result in rolling and spiraling flight paths. In the result section, we experimentally explore the effect of the zigzag pattern on the twist angle.

D. Wing Spanwise Stiffening Through Self-Folding

The zigzag folding pattern also contributes to generating a structural reinforcing effect, as demonstrated in [16]. Consistent with the definition of fold angle θ (Fig. 2e) and the number of zigzag folds n_f (Fig. 2b) the wing's flexural rigidity EI as a function of θ and n_f for a paper of thickness t can be approximated as follows:

$$EI(\theta, n_f) = E_l \frac{wt}{12}\left[t^2 \cos^2\left(\frac{\theta}{2}\right) + \frac{w^2}{(n_f+1)^2}\sin^2\left(\frac{\theta}{2}\right)\right], \quad (2)$$

where $w \simeq 39$ mm is the pre-folding wing width (Fig. 2b) and E_l is the equivalent elastic modulus of the paper parallel to the wing sweep direction. Following this equation, a 30-degree, 5-fold zigzag folding pattern results in a remarkable 422-fold EI increase for an 82 µm-thick paper sheet, verifiable with finite-element analysis (code available at [28]). While the study of the aeroelastic behavior of the glider and the optimization of its stiffness is beyond the scope of this study, our flight tests revealed that low stiffness configurations (i.e., d = 1 mm) frequently transitioned to the anti-symmetric state under aeroelastic loads, resulting in reduced flight time (refer to Section III-C)

III. Exerimental Results

The following sections present the folding and biodegradability tests conducted on different paper varieties and the results of the experimental analysis on the design of the folding pattern and its influence on flight performance.

A. Characterization of Self-Folding

We have tested the inkjet printing method on five different paper varieties, including three types of tracing papers with thicknesses of 50 µm, 82 µm, and 94 µm, a 270 µm-thick potato starch wafer paper, and a 30 µm-thick rice paper. All the paper varieties successfully self-folded along printed creases. Among them, the 82 µm-thick tracing paper was chosen for constructing the gliders as a compromise between weight, flexural rigidity, and strength. The potato starch paper was excluded because its high thickness restricts the folding angle, while the rice paper is suitable only for printing miniaturized structures because of its low mechanical strength and high sensitivity to humidity.

The folding of the 82 µm tracing paper is then further studied by determining the unconstrained folding angle θ as a function of the printing line width d. To this aim, single straight lines are printed across the width of rectangular samples, and the folding angle is measured from photographs with ImageJ.

The tracing paper has a primary cellulose fiber direction along which the ink induces higher bending and thereby achieves a larger folding angle [29]. Therefore, for each d tested, five samples are printed parallel to the fiber direction

and five perpendicularly. Test results plotted in Fig. 3 confirm this difference. In addition, results underline a strongly linear region for $d \geq 0$ .75 mm. Linearity implies that the fold width distributes over an arc of a circle of constant radius of curvature ρ for all $d \geq 0$ .75 mm, following Equation 3.

$$\theta(d) = \frac{180^\circ}{\pi} \frac{d}{\rho} \tag{3}$$

Equation 3 is used to determine the resulting radii of curvature are $\rho_{\parallel}$ = 1.6 mm and $\rho_{\perp}$ = 6.3 mm, respectively for folds parallel and perpendicular to the fiber direction. To that purpose, a zero-intercept linear fitting is necessary, which has lower values of R-squared: $r^2_{\parallel}$ = 0.978 and $r^2_{\perp}$ = 0.944. These values enable the use of Equation 3 to predict the target folding angle based on the selected crease width.

Owing to the difference in folding radii observed above, during fabrication, the glider patterns were aligned with their wingspan perpendicular to the primary fiber direction. This maximizes the chordwise contraction caused by the zigzag folding pattern and therefore the wing twisting effect described in Section II-C.

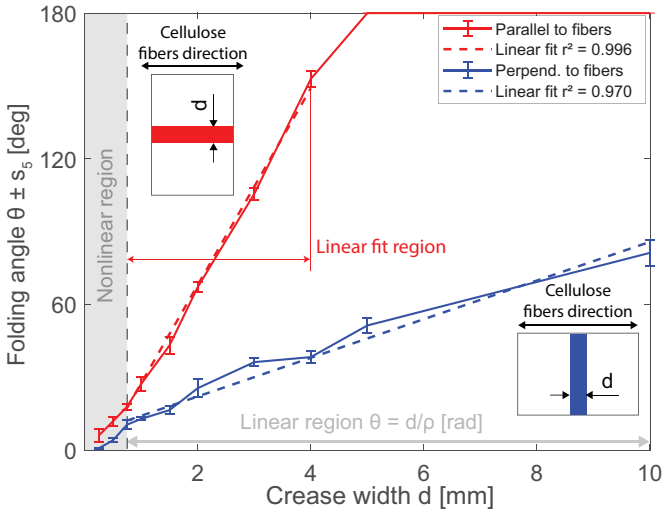

Fig. 3. Characterization of the folding angle θ on 82 µm-thick tracing paper parallel and perpendicular to the fiber direction. Error bars at $\pm s_5$, with s_5 sample standard deviation computed over the five samples. Linear fit for the parallel direction for $d \in [0.75, 4]$ mm due to complete folding at 180° for $d \geq 5$ mm.

B. Biodegradability Tests

The biodegradability of the five types of papers is quantitatively assessed through a soil burial test, which is a common method used in biodegradability studies [30]. Samples of 25 mm × 25 mm were enclosed in 150 µm Nylon mesh bags and buried in soil, which is watered twice a week to maintain sufficient moisture. Weekly, a sample is extracted from the soil, rinsed twice in still de-ionized water, and dried at 40 °C in a ventilated oven for one hour. After drying, the residual mass of the sample is removed from the bag and weighed. Each data point corresponds to a distinct sample due to the destructive measurement. As a benchmark, a tea bag filled with tea leaves was also included in the experiment. The weekly decomposition rate r_{dec} is calculated by comparing the sample's mass with its pre-burial value.

Biodegradable masses follow an exponential decay function as described in [31]. Fig. 4a, reports the percent decomposition rate, including the raw data points and the best-fitting exponential decomposition rate profile r_{dec} as defined in Equation 4:

$$r_{dec}(t) = a(1 - e^{-kt}), \tag{4}$$

where a is the labile fraction of each decomposing mass [31], k the decomposition rate constant, and t the time since burial. The best-fitting values of labile fraction are a = 0.99 for all the tracing paper types, a = 1 for the potato starch and rice paper, and a = 0.8 for the green tea leaves. Fig. 4b shows the sequence of pictures of the residual mass for each sample.

From the test results, all the tested paper varieties have reached significant, if not complete, degradation after 15 weeks of burial in moist soil. Because the rice paper is water soluble, no residual traces of the rice paper were observed since week one. The benchmark decomposition profile obtained with green tea matches reference results of previously published research [31], validating the experiments.

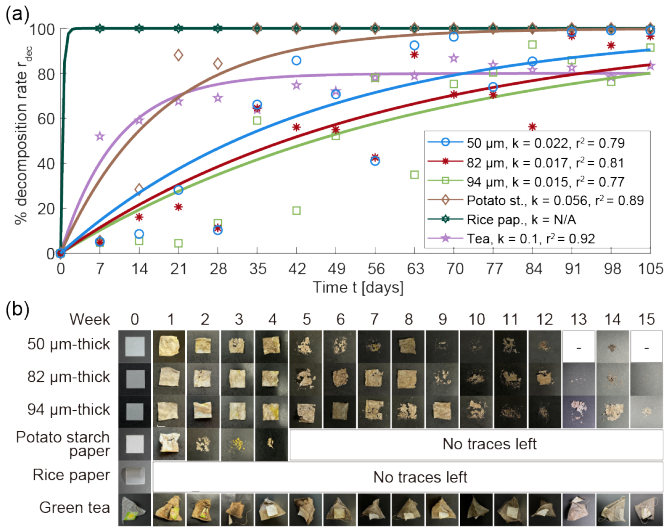

Fig. 4. Biodegradability test different paper varieties. (a) Measured decomposition rate r_{dec} at a weekly sampling rate and exponential fit. The decomposition rate constant k is indicated in days^{-1}, while the best-fitting labile fractions of the decomposing masses are a = 0.99 for tracing paper, a = 1 for potato starch and rice paper, a = 0.85 for green tea. For the rice paper, k and R-squared values are omitted due to the lack of significant data points. (b) Photographs of the residual mass of each sample extracted. Empty cells correspond to an undetectable residual mass.

C. Wing Twist

As previously discussed in Section II-C, twisting of the wing is induced by the bending of wingtips into winglets that restrict the chordwise shrinkage induced by the zigzag folding pattern. The twist angle Φ therefore depends on the amount of shrinkage, which can be adjusted by varying the unconstrained zigzag folding angle θ. Coherently with the geometrical design constraints defined in Section II-A, we

fabricated gliders with 82 µm-thick tracing paper varying two design parameters: the number of creases across the chord n_f, and the crease width d (Fig. 2b).

To study the effect of n_f on Φ, we fabricated gliders with n_f = 3, 5, and 7 equally-spaced creases across the chord, and all the creases have a width of d = 2 mm. Only odd values of n_f are tested because preliminary flight tests evidenced that valley folds near both wing edges are a necessary condition for longitudinal stability. Fig. 5a shows a qualitative comparison of Φ as a function of n_f. Based on observations, the wing twist has a direct relationship with n_f due to the greater number of deformed folds contributing to an increase in the internal energy. To study the dependence of Φ on d as a parameter, we fix n_f = 5, which shows an intermediate wing twist. For higher values of n_f, the smaller gap between folds makes the wing geometry more sensitive to pattern alignment errors between the two printing sides. Increasing n_f also has a detrimental effect on the wing stiffening (Equation 2).

Five samples for each crease width d of 1 mm, 2 mm, and 3 mm were then fabricated with fixed n_f = 5, and the arising twist angle Φ was measured. Fig. 5b shows qualitative pictures of the wing twist angles obtained this way. By using a 3D printed measurement support to fix both the wingtips in the symmetric state, the angle of the root chord is measured to determine Φ. The photograph in Fig. 5c illustrates the measurement setup and procedure.

Results are plotted in Fig. 5c, showing the direct influence of d on Φ. According to Equation 3, the unconstrained fold angle of the zigzag pattern is expected to increase linearly with d. In the presence of the kinematic constraint at the wingtips, this directly correlates with greater pattern distortion and values of internal energy, thus explaining the direct relationship with Φ. Additionally, larger values of d lead to a more-than-linear increase in the sample standard deviation s_5 of Φ, probably due to the larger non-linearity and reciprocal interaction between adjacent folds. Modulation of crease width in the tested range therefore provides a sufficiently repeatable method to adjust flight characteristics through wing twist.

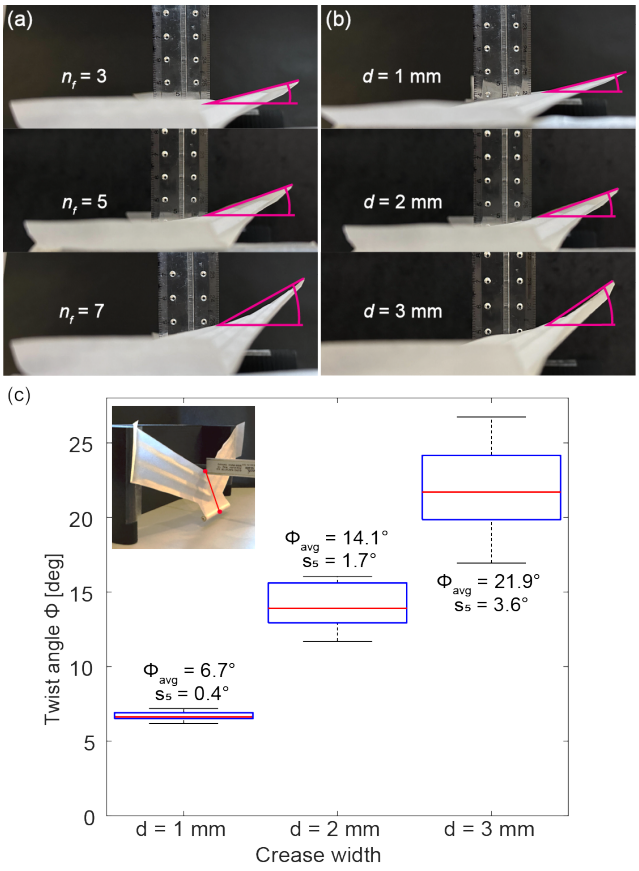

Fig. 5. Effect of pattern parameters on the wing twist angle Φ. (a) Observation of twist as a function of the number of folds n_f with fixed crease width d = 2 mm. (b) Observation of twist as a function of d with fixed n_f = 5 (qualitative). (c) Measurement results of Φ at d = 1 mm, 2 mm, and 3 mm. The red line is the median angle, box limits are the 25th and 75th percentiles, and whiskers are the extremes of the measurement.

D. Impact of Wing Twist and CG Position on Flight Time in Still Atmospheric Conditions

Similar to seed dispersal in nature, prolonged suspension in mid-air leads to longer exposure to wind and thence higher dispersal distance from a given deployment height. The flight performance of the three designs with different crease widths is therefore evaluated for different positions of the CG based on the total flight duration. The gliding tests were conducted releasing the gliders oriented nose-down from a height of 2.5 m, as illustrated in Fig. 6a. An electromagnetic release system ensured the repeatability of the initial release conditions. The tests were conducted indoors in still atmospheric conditions with negligible wind and turbulence.

Five glider samples for each crease width of 1 mm, 2 mm, and 3 mm and n_f = 5 were fabricated for the gliding experiments as discussed in the last section. Due to the variability of the wing twist obtained across samples of the same crease width, for each width, we selected the sample with the median wing twist for the experiments. To this aim, we tested the flight duration with 16 different CG positions relative to the AC (d_{CG}). The distance d_{CG} is adjusted by trimming the length l_c of the front coil by 10 mm each time as discussed in Section II-B. For each value of l_c, the gliding test is repeated three times to assess the variability. Using 81 µm tracing paper, a coil-less glider weighs 0.79 g, and each 10 mm-increment in the nose coil length l_c adds 48 mg of mass to the platform. The maximum glider mass, corresponding to $l_{c,max}$ = 190 mm, peaks at 1.7 g.

Fig. 6b shows the results of the flight tests. The glider with d = 2 mm shows the longest-lasting flight at all values of l_c, with a maximum sample average of 3 s across the three tests at the optimal coil length l_c^* = 80 mm (corresponding to a d_{CG} = 19.6 mm), which also results to be the optimal length for the glider with d = 3 mm. All the gliders with $l_c < 50$ mm stalled and vertically fell with a tumbling motion, with flight duration dominated by drag. For the glider with d = 1 mm, this phenomenon is observed for $l_c < 60$ mm, therefore l_c = 60 mm is the optimal length that still guarantees a gliding

behavior for this glider.

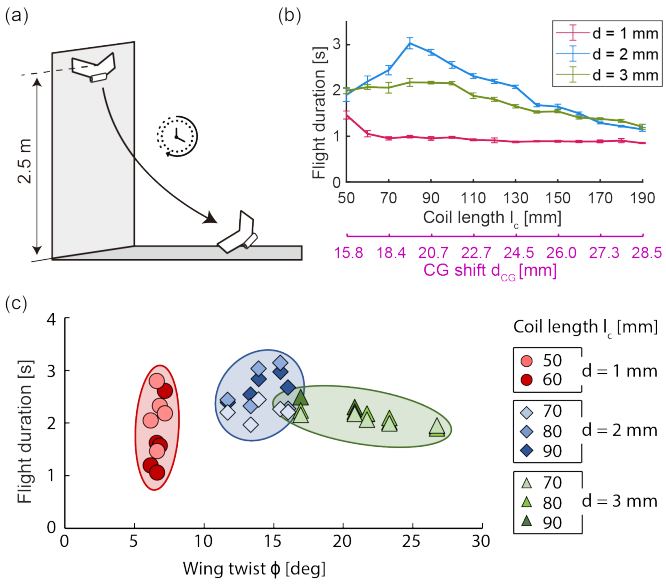

Fig. 6. Indoor gliding tests. (a) Test setup. (b) Effect of l_c, and corresponding d_{CG} on flight duration of the glider with median wing twist Φ for each d = 1, 2, 3, determining the optimal coil length l_c^*; error bars at $\pm$ sample standard deviation. (c) Flight duration of all the glider samples tested at coil lengths l_c^* + 10 mm, l_c^*, and – except for d = 1 mm – to l_c^* - 10 mm. Effects on the flight duration of intra- and inter-class twist angle Φ variability across samples is put in evidence by the horizontal axis.

To assess the repeatability of flight duration, all the samples printed for the wing-twist study (Fig. 5c) are tested in the neighborhood of the optimal coil length determined above. Defining l_c^* the optimal coil length determined above for each crease width, all five gliders are trimmed down to l_c^* + 10 mm, l_c^*, and to l_c^* - 10 mm and the tests are repeated. Their flight duration is measured with the same drop-test procedure.

Based on the results plotted in Fig. 6c, the flight duration of gliders with d = 1 mm shows the highest intra-class variability, with a sample standard deviation of 0.60 s, despite their low variability in the wing twist angle. This phenomenon can be explained by the lower stability of the symmetric twisted wing twist exhibited by gliders with d = 1, which led to more frequent state transitions under the effect of aeroelastic loads. The gliders with d = 2 mm and 3 mm exhibit more consistent flight duration, with sample standard deviations of 0.35 s and 0.16 s, respectively. By observation of flight behavior, the gliders with a 3 mm crease are subject to a shorter average flight duration than the 2 mm ones since the higher wing twist induces more drag than optimal, making them sink faster. Based on the tested gliders, a design with a crease width of 2 mm and l_c^* = 80 mm, which corresponds to d_{CG} = 19.6 mm, demonstrates superior performance in a still atmosphere.

IV. Deployment of Biodegradable Gliders

To showcase the remote deployment of the proposed gliders, we designed a remotely controlled release device capable of carrying and releasing up to five gliders, demonstrating gliders' dispersal in an outdoor setting.

A. Remotely Controlled Release System

The release system comprises a fixed rear rack, a rotating front rack actuated by a servomotor, and an attachment carbon-fiber composite rod (Fig. 7a-c). The racks are laser-cut from 1 mm-thick FR4 glass-fiber reinforced polymer (GFRP) plates. The rear rack features five slits that permit the insertion of gliders' backs. The front rack presents five circular grooves with a 2.6 mm radius designed to hold the nose coil of each glider. Constructed with two layers of GFRP separated by 6 mm-long rubber spacers, the front rack limits glider rotation, preventing unintended releases against wind gusts and aerodynamic loads. The front rack exerts compression on all gliders at the level of the root chord, ensuring that the state with symmetric wing twist is maintained. Gradually opening the front rack angle initiates the sequential bottom-up release of the stacked gliders. The whole release system weighs 97 g, making it an admissible payload for mid-size consumer-grade quadrotors.

B. Revised Glider Design for Outdoor Dispersal

As discussed in Section III-D, the indoor gliding tests determine the best-performing self-folding design progressively reduces the CG-to-AC distance d_{CG} until the longest flight duration is achieved. However, a shorter d_{CG} increases the glider's susceptibility to atmospheric turbulence, particularly near the downwash of the rotorcraft used for their deployment to the environment. Through preliminary release tests, unstable roll oscillations emerged in gliders fabricated following the optimal glider design (l_c = 80 mm), causing them to fall fast near the release location. By increasing l_c – and hence d_{CG} – , the resulting higher flight speed increments roll stability at the expense of shorter gliding duration. We incremented l_c up to 140 mm, where stable gliding was eventually achieved from a release height of 25 m. Therefore, a glider design with a 2 mm crease width and a d_{CG} = 25.2 mm (corresponding to l_c = 140 mm) was selected for the outdoor dispersal experiments.

C. Outdoor Dispersal Experiments

We mounted the release system on a DJI Mavic 3 Classic, such that the rearmost points on the glider wingtips are farther than one propeller diameter (here, 240 mm), and performed deployment experiments from a 15 m altitude. We demonstrated the successful sequential release of four gliders in a single launch mission (Fig. 7d) and measured the gliding duration and distance covered by six gliders released during two different deployments, with three gliders each. Fig. 7e shows snapshots and a qualitative path of the three gliders released in one of these two deployments. The atmospheric wind conditions were calm, with average wind speeds lower than 4 km/h measured at a local weather station at a 10 m height. Accurate GPS coordinates of the gliders' landing positions are logged by a DJI Mini 3 Pro by flying and

hovering above each glider's landing spot and later importing them on Google Earth (see Fig. 7f).

Across the six measured glides, the maximum distance is 30 m, the sample mean is 16.5 m, and the corrected sample standard deviation is 8.25 m. We define the gliding distance ratio DR as the ratio between the shortest-path horizontal distance from release to landing location and the release altitude for each glider. In terms of DR, the six glides achieve a maximum DR_{max} = 2, sample mean $\overline{\mathrm{DR}}$ = 1.1, and corrected sample standard deviation $s(\mathrm{DR})$ = 0.55. The latter captures well the ability of the biodegradable gliders to disperse in the environment as higher $s(\mathrm{DR})$ values imply that the landing locations of gliders released from a determined altitude and position are subject to higher variability.

Environmental conditions with stronger and persistent wind will further contribute to increasing the distance ratio, adding to the DR obtained through gliding. Should strong winds displace the whole batch of released gliders, the observed variability in their gliding paths would still provide sufficient dispersal.

V. Conclusions

We propose a method for the fabrication of self-folding biodegradable flyers from flat sheets of paper. Using print-induced paper folding via inkjet printing, we demonstrate the fabrication of gliders with 3D shapes featuring the necessary aerodynamic, inertial, and structural properties for a stable gliding behavior. Longitudinal gliding stability is obtained by balancing the effects of the longitudinal position of the CG and the angle of twist of the wing. The interplay of these two parameters influences the gliding duration in indoor tests. By shifting forward the CG position to increase the glide stability against air turbulence near the release platform, we demonstrated and characterized the outdoor deployment and dispersal capabilities of the proposed gliders.

In the future, our goal is to streamline the design process from printing patterns to evaluating flight performance. This involves modeling the folding process induced by inkjet printing and utilizing aerodynamic simulations to explore the aerodynamic characteristics of the glider in different atmospheric conditions. Of particular interest is investigating the impact of sharp geometries and local corrugations on flow separation. These features can be beneficial for enhancing turbulence resilience and flight efficiency [32], [33].

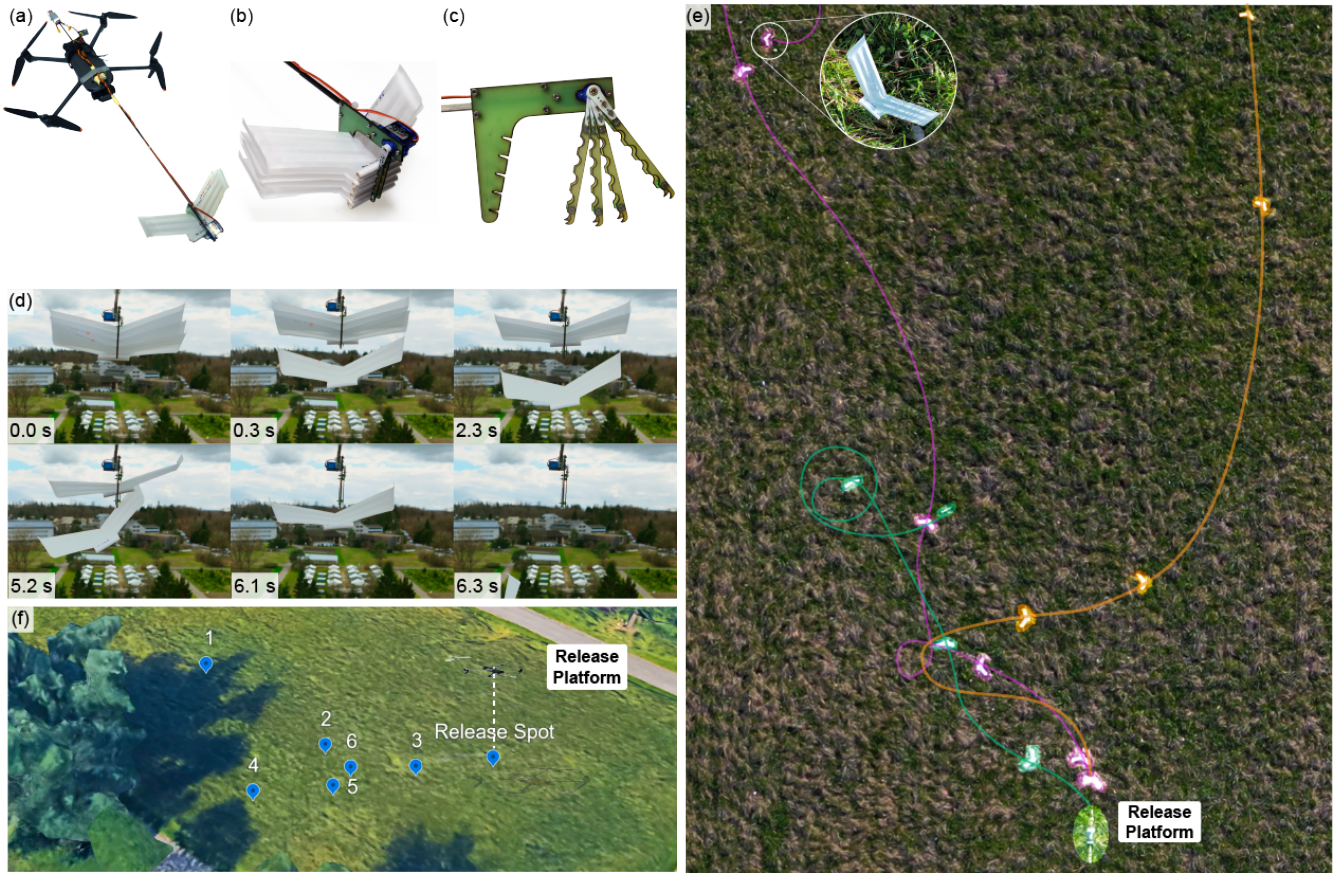

Fig. 7. Outdoor glider deployment. (a-b) Release platform (DJI Mavic 3 Classic) with the servomotor-controlled release system for up to five gliders. (c) Detailed view of the opening of the release system. (d) Sequential bottom-up release of four gliders in a single outdoor deployment test. (e) Snapshots of a top-view deployment of three, color-coded gliders in a single deployment from a 15 m height. The colored trajectories qualitatively represent the path followed by the gliders. (f) Overview of the release and landing locations of the six tested glides through GPS coordinates in Google Earth.

For environmental monitoring applications, the paper glider can be functionalized using minimalist methods including chromogenic paint, such as thermochromic, hydrochromic, and photochromic paints, which vary in color when exposed to temperature variation, moisture, and UV radiation, respectively. For applications such as forest restoration, plant seeds can be incorporated into the paper to enable artificial seed dispersal. We also envision a maneuverable platform capable of following differentiated paths actively steering and transitioning between different gliding behaviors, as in [9], exploiting all gliders' stable configurations – with symmetric and asymmetric wing twists. Employing nature-inspired biodegradable actuation systems that react to environmental stimuli, such as light-, temperature-, or moisture-reactive materials [34], [35], would preserve the complete platform's biodegradability.

REFERENCES

[1] M. Seale and N. Nakayama, "From passive to informed: mechanical mechanisms of seed dispersal," *New Phytologist*, vol. 225, no. 2, pp. 653–658, 2020.

[2] I. M. Viola and N. Nakayama, "Flying seeds," *Current Biology*, vol. 32, no. 5, pp. R204–R205, 2022.

[3] K. Johnson, V. Arroyos, A. Ferran, R. Villanueva, D. Yin, T. Elberier, A. Aliseda, S. Fuller, V. Iyer, and S. Gollakota, "Solar-powered shape-changing origami microfliers," *Science Robotics*, vol. 8, no. 82, p. eadg4276, 2023.

[4] B. Mazzolai, T. Kraus, N. Pirrone, L. Kooistra, A. De Simone, A. Cottin, and L. Margheri, "Towards new frontiers for distributed environmental monitoring based on an ecosystem of plant seed-like soft robots," in *Proceedings of the Conference on Information Technology for Social Good*, 2021, pp. 221–224.

[5] D. Luo, A. Maheshwari, A. Danielescu, J. Li, Y. Yang, Y. Tao, L. Sun, D. K. Patel, G. Wang, S. Yang, *et al.*, "Autonomous self-burying seed carriers for aerial seeding," *Nature*, vol. 614, no. 7948, pp. 463–470, 2023.

[6] V. Iyer, H. Gaensbauer, T. L. Daniel, and S. Gollakota, "Wind dispersal of battery-free wireless devices," *Nature*, vol. 603, no. 7901, pp. 427–433, 2022.

[7] D. Wang, Z. Chen, M. Li, Z. Hou, C. Zhan, Q. Zheng, D. Wang, X. Wang, M. Cheng, W. Hu, *et al.*, "Bioinspired rotary flight of light-driven composite films," *Nature Communications*, vol. 14, no. 1, p. 5070, 2023.

[8] B. H. Kim, K. Li, J.-T. Kim, Y. Park, H. Jang, X. Wang, Z. Xie, S. M. Won, H.-J. Yoon, G. Lee, *et al.*, "Three-dimensional electronic microfliers inspired by wind-dispersed seeds," *Nature*, vol. 597, no. 7877, pp. 503–510, 2021.

[9] S. K. H. Win, L. S. T. Win, D. Sufiyan, G. S. Soh, and S. Foong, "An agile samara-inspired single-actuator aerial robot capable of autorotation and diving," *IEEE Transactions on Robotics*, vol. 38, no. 2, pp. 1033–1046, 2021.

[10] P. Pounds and S. Singh, "Samara: Biologically inspired self-deploying sensor networks," *IEEE potentials*, vol. 34, no. 2, pp. 10–14, 2015.

[11] F. Wiesemüller, Z. Meng, Y. Hu, A. Farinha, Y. Govdeli, P. H. Nguyen, G. Nyström, and M. Kovač, "Transient bio-inspired gliders with embodied humidity responsive actuators for environmental sensing," *Frontiers in Robotics and AI*, vol. 9, p. 1011793, 2022.

[12] S. S. Sethi, M. Kovac, F. Wiesemüller, A. Miriyev, and C. M. Boutry, "Biodegradable sensors are ready to transform autonomous ecological monitoring," *Nature Ecology & Evolution*, vol. 6, no. 9, pp. 1245–1247, 2022.

[13] C. Geckeler, B. A. Pizzani, and S. Mintchev, "Biodegradable origami gripper actuated with gelatin hydrogel for aerial sensor attachment to tree branches," in *2023 IEEE International Conference on Robotics and Automation (ICRA)*. IEEE, 2023, pp. 5324–5330.

[14] H.-J. Yoon, G. Lee, J.-T. Kim, J.-Y. Yoo, H. Luan, S. Cheng, S. Kang, H. L. T. Huynh, H. Kim, J. Park, *et al.*, "Biodegradable, three-dimensional colorimetric fliers for environmental monitoring," *Science advances*, vol. 8, no. 51, p. eade3201, 2022.

[15] K. Cikalleshi, A. Nexha, T. Kister, M. Ronzan, A. Mondini, S. Mariani, T. Kraus, and B. Mazzolai, "A printed luminescent flier inspired by plant seeds for eco-friendly physical sensing," *Science Advances*, vol. 9, no. 46, p. eadi8492, 2023.

[16] Y. Fukatsu and H. Shigemune, "Development of self-folded corrugated structures using automatic origami technique by inkjet printing," *Advanced Intelligent Systems*, vol. 4, no. 6, p. 2100260, 2022.

[17] H. Shigemune, S. Maeda, Y. Hara, N. Hosoya, and S. Hashimoto, "Origami robot: a self-folding paper robot with an electrothermal actuator created by printing," *IEEE/ASME Transactions On Mechatronics*, vol. 21, no. 6, pp. 2746–2754, 2016.

[18] H. Shigemune, S. Maeda, E. Iwase, S. Hashimoto, S. Sugano, and H. Sawada, "Programming stepwise motility into a sheet of paper using inkjet printing," *Advanced Intelligent Systems*, vol. 3, no. 1, p. 2000153, 2021.

[19] S. K. Mahadeva, K. Walus, and B. Stoeber, "Paper as a platform for sensing applications and other devices: a review," *ACS applied materials & interfaces*, vol. 7, no. 16, pp. 8345–8362, 2015.

[20] S. Zona. (2011) Alsomitra macrocarpa seed. [Online]. Available: https://www.flickr.com/photos/12017190@N06/5616740256

[21] S. Minami and A. Azuma, "Various flying modes of wind-dispersal seeds," *Journal of theoretical biology*, vol. 225, no. 1, pp. 1–14, 2003.

[22] A. Azuma and Y. Okuno, "Flight of a samara, alsomitra macrocarpa," *Journal of Theoretical Biology*, vol. 129, no. 3, pp. 263–274, 1987.

[23] R. C. Nelson *et al.*, *Flight stability and automatic control*. WCB/McGraw Hill New York, 1998, vol. 2.

[24] D. Tam, J. W. Bush, M. Robitaille, and A. Kudrolli, "Tumbling dynamics of passive flexible wings," *Physical review letters*, vol. 104, no. 18, p. 184504, 2010.

[25] T. Howison, J. Hughes, and F. Iida, "Large-scale automated investigation of free-falling paper shapes via iterative physical experimentation," *Nature Machine Intelligence*, vol. 2, no. 1, pp. 68–75, 2020.

[26] H. Li, T. Goodwill, Z. J. Wang, and L. Ristroph, "Centre of mass location, flight modes, stability and dynamic modelling of gliders," *Journal of Fluid Mechanics*, vol. 937, p. A6, 2022.

[27] N. Obayashi, K. Junge, S. Ilić, and J. Hughes, "Robotic automation and unsupervised cluster assisted modeling for solving the forward and reverse design problem of paper airplanes," *Scientific Reports*, vol. 13, no. 1, p. 4212, 2023.

[28] L. Girardi. (2024) Wing folding rigidity. [Online]. Available: https://github.com/erl-ethz/wing_folding_rigidity.git

[29] D. Naritomi, N. Hosoya, G. Ando, S. Maeda, and H. Shigemune, "Creation of origami-inspired honeycomb structure using self-folding paper," *Materials & Design*, vol. 223, p. 111146, 2022.

[30] D. Briassoulis, A. Mistriotis, N. Mortier, and M. Tosin, "A horizontal test method for biodegradation in soil of bio-based and conventional plastics and lubricants," *Journal of Cleaner Production*, vol. 242, p. 118392, 2020.

[31] J. A. Keuskamp, B. J. Dingemans, T. Lehtinen, J. M. Sarneel, and M. M. Hefting, "Tea bag index: a novel approach to collect uniform decomposition data across ecosystems," *Methods in Ecology and Evolution*, vol. 4, no. 11, pp. 1070–1075, 2013.

[32] M. Di Luca, S. Mintchev, Y. Su, E. Shaw, and K. Breuer, "A bioinspired separated flow wing provides turbulence resilience and aerodynamic efficiency for miniature drones," *Science Robotics*, vol. 5, no. 38, p. eaay8533, 2020.

[33] M. Di Luca, K. Breuer, and S. Mintchev, "Cavities improve the power factor of low-reynolds-number airfoils and wings," *AIAA Journal*, vol. 60, no. 3, pp. 1679–1690, 2022.

[34] M. Seale, A. Kiss, S. Bovio, I. M. Viola, E. Mastropaolo, A. Boudaoud, and N. Nakayama, "Dandelion pappus morphing is actuated by radially patterned material swelling," *Nature Communications*, vol. 13, no. 1, p. 2498, 2022.

[35] Z. Chen, B. Gao, P. Li, X. Zhao, Q. Yan, Z. Liu, L. Xu, H. Zheng, F. Xue, R. Ding, *et al.*, "Multistimuli-responsive actuators derived from natural materials for entirely biodegradable and programmable untethered soft robots," *ACS nano*, vol. 17, no. 22, pp. 23 032–23 045, 2023.